Crystal Structure Control of Binary and Ternary Solid-Solution Alloy Nanoparticles with a Face-Centered Cubic or Hexagonal Close-Packed Phase

Quan Zhang,[*,†] Kohei Kusada,[*,†] Dongshuang Wu,[†] Tomokazu Yamamoto,[‡] Takaaki Toriyama,[‡] Syo Matsumura,[‡,§] Shogo Kawaguchi,[⊥] Yoshiki Kubota,[#] and Hiroshi Kitagawa[*,†]

[†]Division of Chemistry, Graduate School of Science, Kyoto University, Kitashirakawa-Oiwakecho, Sakyo-ku, Kyoto 606-8502, Japan

[‡]The Ultramicroscopy Research Centre, Kyushu University, Motooka 744, Nishi-ku, Fukuoka 819-0395, Japan

[§]Department of Applied Quantum Physics and Nuclear Engineering, Kyushu University, 744 Motooka, Nishi-ku, Fukuoka 819-0395, Japan

[⊥]Japan Synchrotron Radiation Research Insitute (JASRI), SPring-8, 1-1-1 Kouto, Sayo-cho, Sayo-gun, Hyogo 679-5198, Japan

[#]Department of Physical Science, Graduate School of Science, Osaka Prefecture University, Sakai, Osaka 599-8531, Japan

ABSTRACT: The crystal structure significantly affects the physical and chemical properties of solids. However, the crystal structure dependent properties of alloys are rarely studied because controlling the crystal structure of an alloy at the same composition is extremely difficult. Here, for the first time, we successfully demonstrate the synthesis of binary Ru–Pt (Ru:Pt = 7:3), Ru–Ir (Ru:Ir = 7:3), and ternary Ru–Ir–Pt (Ru:Ir:Pt = 7:1.5:1.5) solid-solution alloy nanoparticles (NPs) with well-controlled hexagonal close-packed (hcp) and face-centered cubic (fcc) phases, respectively, through the chemical reduction method. The crystal structure control is realized by precisely tunning the reduction speeds of the metal precursors. The effect of crystal structure on the catalytic performance of solid-solution alloy NPs is systematically investigated. Impressively, all the hcp alloy NPs show superior electrocatalytic activities for the hydrogen evolution reaction in alkaline solution compared with the fcc alloy NPs. In particular, hcp-RuIrPt exhibits extremely high intrinsic (mass) activity, which is 3.1 (3.2) and 6.7 (6.9) times enhancement to the fcc-RuIrPt and commercial Pt/C.

INTRODUCTION

The crystal structure, which is the arrangement of atoms in a solid, is one of the most important parameters affecting the properties of solids.[1] Diamond and graphite are famous allotropes of carbon with cubic and hexagonal structures, respectively. Diamond is a well-known electrical insulator, whereas graphite is a good electrical conductor.[2] Additionally, α-iron has a body-centered cubic (bcc) structure and is ferromagnetic, whereas γ-iron, an allotrope with a face-centered cubic (fcc) structure is nonmagnetic.[3] Therefore, selective control of the crystal structure of materials can be an attractive approach for developing new functional materials.[4–8]

Solid-solution alloy nanoparticles (NPs), in which the constituent atoms mix randomly, have been increasingly studied because of their widespread applications in magnetics, optics, and catalysis.[9–13] These NPs usually adopt one of the three basic crystal structures, fcc, bcc, and hexagonal close-packed (hcp) structures. Controlling the crystal structures of solid-solution alloys with the same composition is a highly challenging task because, once their constituent elements and composition are fixed, most alloys only have one thermodynamically favorable structure over a wide range of temperatures and/or pressures.[14] To date, although a vast number of studies have explored solid-solution alloy NPs, a rational strategy to selectively control their crystal structures is not well developed yet.[15,16] Furthermore, the effect of the crystal structure on the properties of solid-solution alloys is scarcely investigated because of the difficulty in crystal structure control.[17]

In this work, we selectively synthesized the fcc and hcp phases of the RuPt, RuIr, and RuIrPt solid-solution alloy NPs with the same composition and size, by finely tuning the reduction speeds of the metal precursors through a chemical reduction method. Synchrotron X-ray diffraction (XRD), atomic-resolution scanning-transmission electron microscopy (STEM), and energy-dispersive X-ray spectroscopy (EDX) analysis reveal that the obtained NPs have the typical fcc or hcp solid-solution structures. Furthermore, as a proof-of-concept demonstration, we systematically studied the effects of crystal structure on the catalytic performance through the electrocatalytic hydrogen evolution

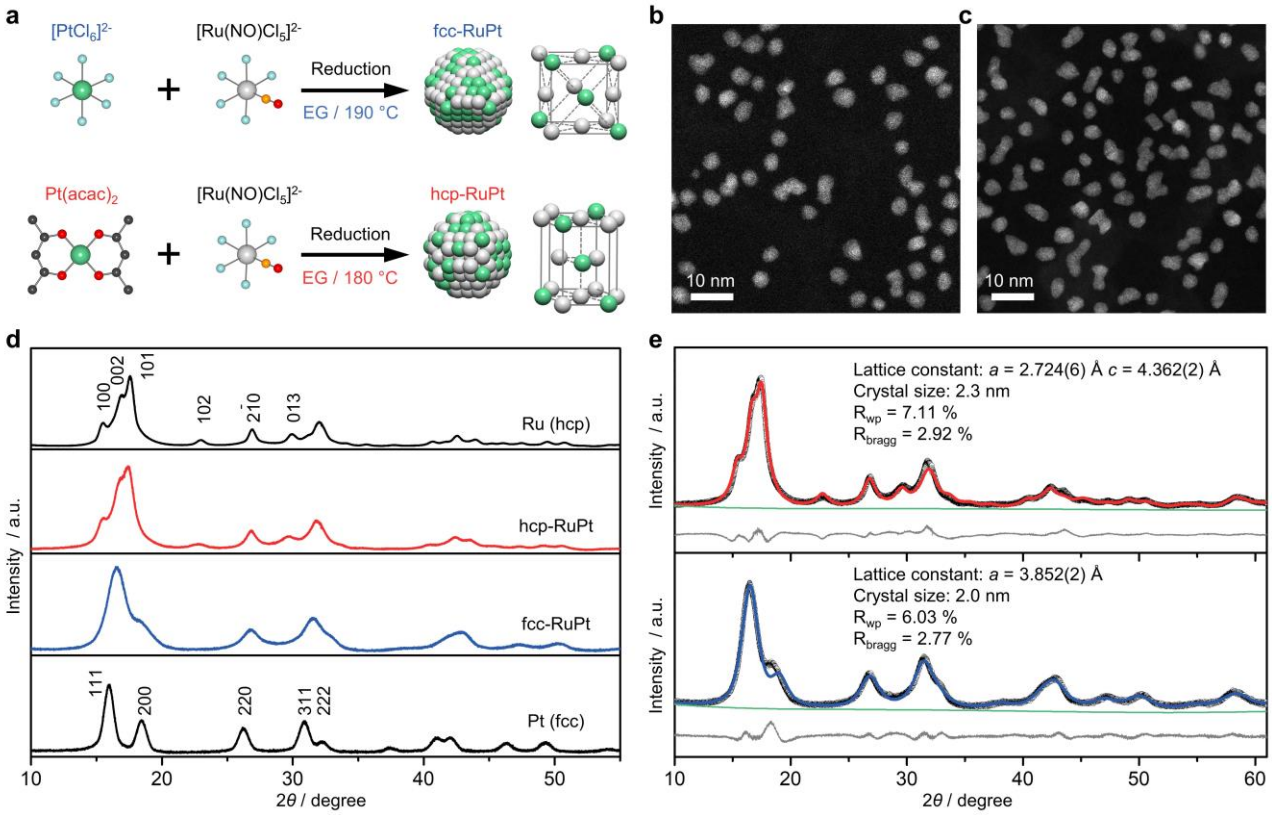

Figure 1. (a) Synthesis scheme of fcc- and hcp-RuPt alloy NPs. The gray, green, light blue, orange, red, and black spheres represent Ru, Pt, Cl, N, O, and C atoms, respectively. H and K atoms are omitted for clarity. **(b)**, **(c)** Low-magnification HAADF-STEM images of fcc- and hcp-RuPt NPs, respectively. **(d)** Synchrotron XRD patterns of the RuPt NPs. The radiation wavelength is 0.630225(2) Å. **(e)** Rietveld refinement analysis of the hcp- and fcc-RuPt alloy NPs. The red and blue curves are the calculated patterns for hcp- and fcc-RuPt alloy NPs, respectively. The tested XRD patterns are shown as black circles. The difference profiles and the background profiles are shown as gray and green curves, respectively.

reaction (HER). The hcp alloy NPs show a significant enhancement in electrocatalytic activities for HER in alkaline over the fcc NPs in all alloy systems, indicating that the HER catalytic performance strongly depends on the crystal structure. In particular, the hcp-RuIrPt NPs exhibits an extremely high activity with a low overpotential (η) of of 9.4 mV at 10 mA cm^{-2}, high turnover frequency (TOF) of 2.94 s^{-1}, and mass activity (j_{mass}) of 877.5 A g^{-1} at 30 mV, which is one of the best reported alloy catalysts for the alkaline HER.

RESULTS AND DISCUSSION

Syntheses of fcc- and hcp-RuPt NPs. We synthesized the RuPt solid-solution alloy NPs through polyol reduction methods (Figure 1a). To obtain the fcc-RuPt NPs, the aqueous solution of potassium pentachloronitrosylruthenate(II) ($K_2Ru(NO)Cl_5$) and hexachloroplatinic(IV) acid hexahydrate ($H_2PtCl_6{\cdot}6H_2O$) with a molar ratio of 7:3 was used as the metal precursor solution. The fcc-RuPt NPs was synthesized by slowly dropping the metal precursor solution into a hot ethylene glycol (EG) solution with polyvinylpyrrolidone (PVP) as the protective agent. During the whole process, the reaction temperature was kept at around 190 °C. The synthesized NPs were collected by centrifugation. By contrast, to obtain hcp-RuPt NPs, $K_2Ru(NO)Cl_5$ and platinum (II) acetylacetonate ($Pt(acac)_2$) were chosen as metal precursors. First, the metal precursor solution was prepared by dissolving $K_2Ru(NO)Cl_5$ and $Pt(acac)_2$ with a molar ratio of 7:3 in triethylene glycol (TEG). Then, the hcp-RuPt NPs were synthesized by slowly dropping the metal precursor solution into the hot EG solution containing PVP. During the reaction, the temperature was kept at around 180 °C. Last, the synthesized NPs were also collected by centrifugation. The details of the synthesis conditions are shown in Supporting Information (Table S1).

The crystal structures of the synthesized alloy NPs were investigated by synchrotron XRD at the beamline BL02B2, SPring-8.[18] The two synthesized RuPt NPs have different types of XRD patterns (Figure 1d). The Rietveld refinement results showed that RuPt NPs synthesized with $H_2PtCl_6{\cdot}6H_2O$ and $K_2Ru(NO)Cl_5$ form an fcc structure, whereas the other RuPt NPs synthesized with $Pt(acac)_2$ and $K_2Ru(NO)Cl_5$ form an hcp structure (Figure 1e). The fcc-RuPt had a lattice constant of 3.852(2) Å, smaller than that of the Pt NPs (a = 3.916(6) Å, Figure S1). The lattice constants of hcp-RuPt were a = 2.724(6) and c = 4.362(2) Å, respectively, which were larger than those of the Ru NPs (a = 2.706(1) Å, c = 4.300(4) Å, Figure S2). The lattice parameter values were consistent with those of the ideal solid-solution alloy values calculated from Vegard's law (Table S2).[19] These results strongly suggest the formation of

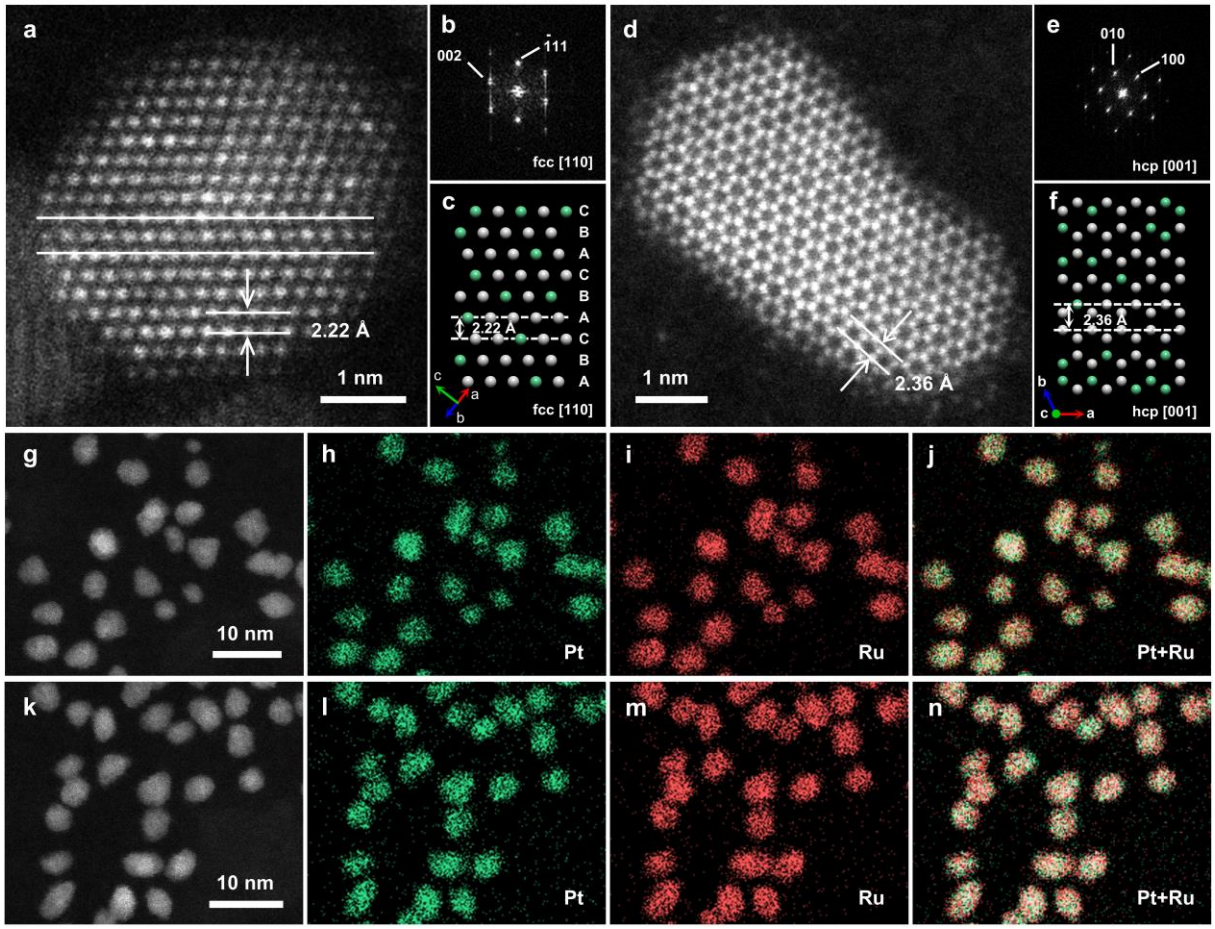

Figure 2. Structure characterization of fcc- and hcp-RuPt alloy NPs. **(a)** Atomic resolution HAADF-STEM image of an fcc-RuPt NP. The white lines in **(a)** show the twin boundaries. **(b)** The relevant fast Fourier transform (FFT) pattern of **(a)**. **(c)** Ideal fcc atomic arrangement constructed by the Rietveld refinement result. **(d)** Atomic resolution HAADF-STEM image of an hcp-RuPt NP. **(e)** The relevant FFT pattern of **(d)**. **(f)** Ideal hcp atomic arrangement constructed by the Rietveld refinement result. **(g)–(j), (k)–(n)** STEM-EDX maps of fcc- and hcp-RuPt alloy NPs.

fcc and hcp RuPt solid-solution alloy NPs. Furthermore, the thermal stability of the obtained alloy NPs was confirmed by in situ XRD (Figures S3 and S4). Both phases were maintained at 873 K.

The atomic ratios of Ru and Pt in both of the prepared NPs were confirmed as Ru:Pt = 7:3 by EDX and X-ray fluorescence (XRF) (Table S3). These results were consistent with the nominal ratios of the alloy NPs. Furthermore, the transmission electron microscopy (TEM) and low-magnification high-angle annular dark-field (HAADF) STEM images show that the size distributions of the synthesized NPs are quite similar, at 3.7 ± 0.3 nm for fcc-RuPt and 3.6 ± 0.4 nm for hcp-RuPt (Figures S5, and 1b, c).

The synthesized NPs were further characterized by atomic-resolution HAADF-STEM to observe the atomic arrangements directly. The NP in Figure 2a presents a clear atomic arrangement with ABCABC stacking, typical of an fcc lattice viewed from the [110] direction. The lattice spacing of the fcc (111) planes is 2.22 Å, which is consistent with the result obtained by the Rietveld refinement (Figure 2c). The corresponding fast Fourier transform (FFT) pattern (Figure 2b) shows a characteristic fcc structure viewed from the [110] direction, confirming the fcc structure of the NP. The fcc structure was also confirmed by other NPs (Figure S6). The atomic arrangements of hcp-RuPt NPs were also investigated by STEM images (Figures 2d-f, and S7). A typical hcp atomic arrangement, as viewed from the [001] direction of a typical hcp structure, is observed in Figure 2d. This structure is also consistent with the ideal atomic arrangements constructed by the Rietveld refinement result with a (100) lattice spacing of 2.36 Å. (Figure 2f). The FFT pattern in Figure 2e shows a characteristic diffraction along the [001] zone axis of an hcp structure. The EDX maps show the random and homogeneous distributions of Ru and Pt atoms in each NP, indicating the solid-solution structures of both fcc- and hcp-RuPt NPs (Figures 2g–n). The EDX line scans further clearly show homogeneous Ru and Pt distributions in the NPs without any surface segregation (Figure S8).

The electronic states of the alloy NPs were confirmed by X-ray photoelectron spectroscopy (XPS) (Figure S9 and Table S4). The Pt 4*f* peaks of both alloys shifted to a lower energy than Pt NPs. In contrast, the Ru 3*p* peaks of both alloys shifted to higher energy compared with the Ru NPs. These results indicate that electron transfer occurs from Ru to Pt in the alloy NPs because of the formation of the solid- solution alloys. The peak positions of the two elements in

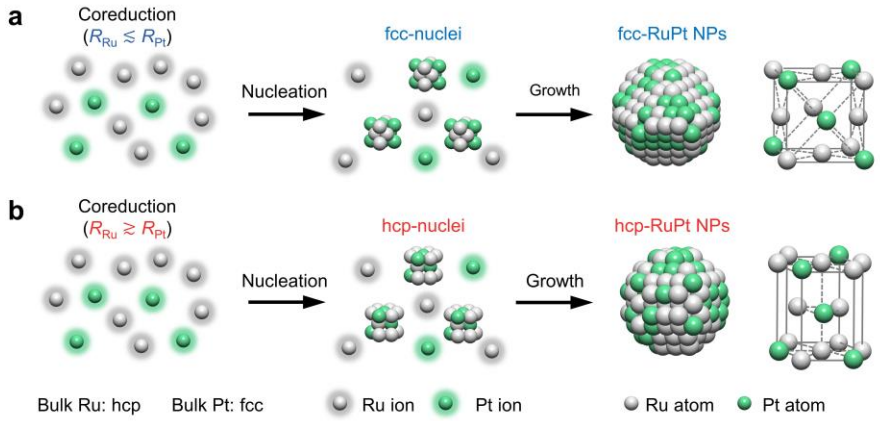

Figure 3. Scheme for crystal structure control of **(a)** fcc- and **(b)** hcp-RuPt alloy NPs. R_{Ru} and R_{Pt} denote the reduction speeds of the Ru and Pt precursors, respectively.

the different crystal structures showed negligible differences, suggesting that both fcc and hcp alloy NPs presented similar homogenous solid-solution structures. We further calculated the compositions of each alloy from their XPS peak area. The results were consistent with the EDX and XRF analyses, further confirming the homogeneous solid-solution structure of the synthesized alloy NPs (Table S5).

Mechanism of crystal structure control. In general, to obtain a solid-solution structure through chemical reduction methods, concurrent reduction of different metal precursors is preferred.[20–22] Here, concurrent reduction means that the difference in reduction speeds of the metal precursors needs to be adjusted within a suitable range.[23, 24] If the difference in their reduction speeds is too large, core-shell or other phase-separated structures will be formed.[24–26] Xia, et al. has quantitatively investigated the effect of reduction speed of metal precursors on the formation of alloys with different structure. PdPt bimetallic NPs with a core-shell structure were obtained when the reduction speed of the Pd precursor is about 4–5 times larger than that of the Pt. When the difference in reduction speed is smaller than a factor of 4, PdPt alloy NPs with a solid-solution structure were obtained.[24] That said, a small difference in reduction speed allows the formation of an alloy with a solid-solution structure.

According to the classic nucleation theory, the crystal structure of an alloy can be governed by its nuclei structure.[23, 27] Due to the existence of small difference in reduction speed between the metal precursors during the concurrent reduction, we suppose that the nuclei structure may be dominated by the metal element reduced relatively faster than the other. Given this situation, it would be considered that the Pt precursor may be reduced relatively faster than the Ru precursor for the synthesis of fcc-RuPt, because Pt usually adopts the fcc structure. Likewise, for the synthesis of hcp-RuPt, the Ru precursor may be reduced relatively faster than the Pt precursor, because Ru usually adopts the hcp structure (Figure 3). We, therefore, investigated the reduction processes of the metal precursors under similar reaction conditions for the syntheses of alloy NPs with ultraviolet visible (UV-vis) spectroscopy (see the experimental details in Supporting Information, Figure S10). The reductions of H_2PtCl_6 and $K_2Ru(NO)Cl_5$ take around 30 and 60 s, respectively, confirming a slightly faster reduction of H_2PtCl_6 during the synthesis of fcc-RuPt. In contrast, the reductions of $K_2Ru(NO)Cl_5$ and $Pt(acac)_2$ take around 90 s and 180 s respectively, confirming a slightly faster reduction of $K_2Ru(NO)Cl_5$ during the synthesis of hcp-RuPt. From these results, we suppose that the crystal structure control of an alloy NP can be realized by finely tuning the reduction speeds of the metal precursors.

Syntheses of fcc- and hcp-RuIr NPs. To verify our crystal structure control strategy, we synthesized RuIr alloy NPs in a similar way (Figure S11). The details of the synthesis conditions are shown in the experimental part of Supporting Information (Table S1). We succeeded in the crystal structure-controlled syntheses of fcc- and hcp-RuIr alloy NPs (Ru:Ir = 7:3).

The structures of fcc- and hcp-RuIr alloy NPs were confirmed by synchrotron XRD patterns, Rietveld refinements (Figures S12–S15, Table S6), and atomic resolution STEM-EDX analysis (Figures S16 and S17). In addition, the in situ XRD measurements confirmed the stability of the fcc- and hcp-RuIr solid-solution alloy structures (Figures S18 and S19). TEM images of RuIr show that both types of NPs had similar particle sizes of approximately 3 nm (Figure S20). The atomic ratios of Ru, and Ir in the prepared NPs were confirmed by both EDX and XRF (Tables S7). The results of XPS suggested electron transfer from Ru to Ir in both fcc and hcp alloys (Figure S21, Table S8). The compositions of RuIr NPs were also calculated from XPS peak areas (Table S9). The successful syntheses of fcc- and hcp-RuIr alloy NPs indicate that our crystal structure control strategy can be used in other binary alloy systems.

Syntheses of ternary fcc- and hcp-RuIrPt NPs. Our synthesis method was applied to multicomponent solid-solution alloys. Here, as the first example, we synthesized ternary fcc- and hcp-RuIrPt alloy NPs (Figure 4a). Alloys with fcc and hcp structures were synthesized by replacing half of the Pt precursor with hydrogen hexachloroiridate(IV) hydrate ($HIrCl_6 \cdot xH_2O$), while keeping the other conditions consistent with the procedure for the synthesis of fcc- and hcp-RuPt (see the experimental details in Supporting Information and Table S1).

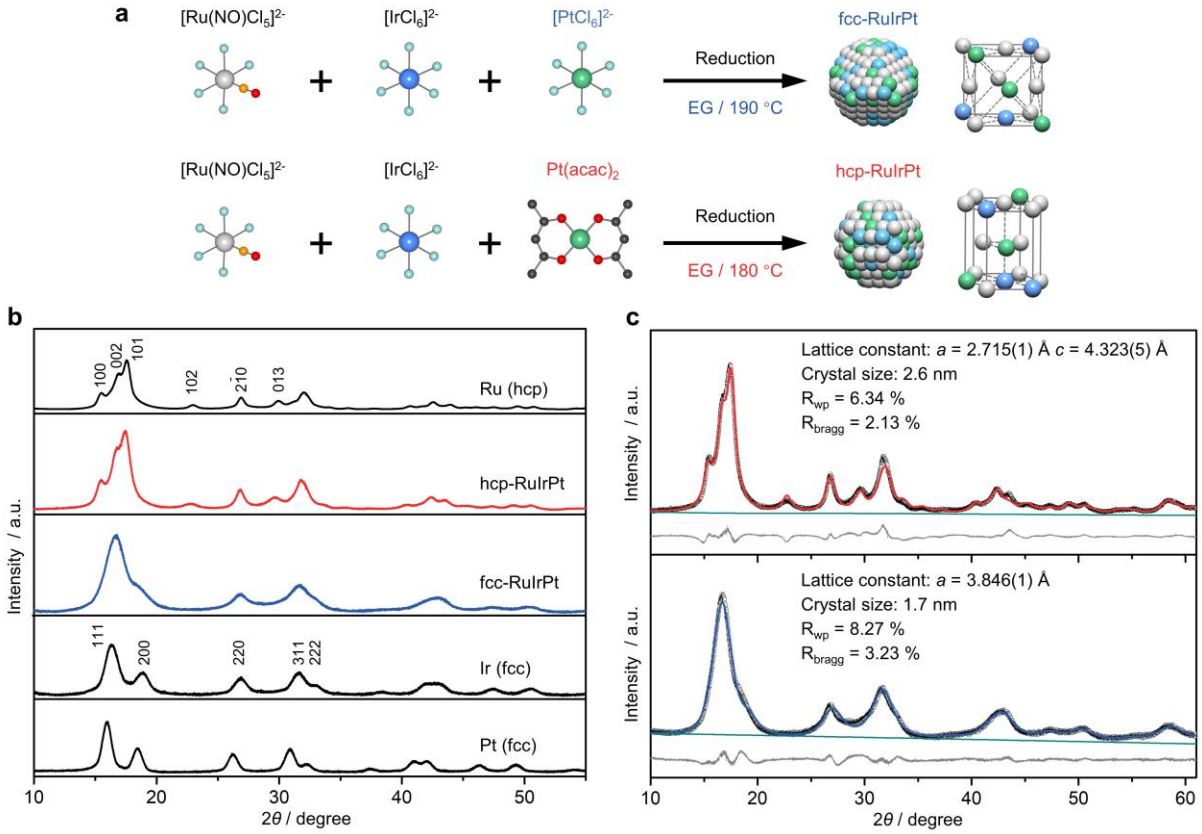

Figure 4. (a) Synthesis scheme of fcc- and hcp-RuIrPt alloy NPs. The gray, blue, green, light blue, orange, red, and black spheres represent Ru, Ir, Pt, Cl, N, O, and C atoms, respectively. H and K atoms are omitted for clarity. **(b)** Synchrotron XRD patterns of the RuIrPt NPs. The radiation wavelength is 0.630225(2) Å. **(c)** Rietveld refinement analysis of the hcp- and fcc-RuIrPt alloy NPs. The red and blue curves are the calculated patterns for hcp- and fcc-RuIrPt alloy NPs, respectively. The tested XRD patterns are shown as black circles. The difference and the background profiles are shown as gray and green curves, respectively.

Synchrotron XRD patterns and the related Rietveld refinement results confirmed the formation of fcc and hcp RuIrPt solid-solution alloy structures (Figures 4b, c, Table S10). Furthermore, both fcc- and hcp-RuIrPt alloy NPs showed good stability during in situ XRD measurements (Figures S22, S23). According to the TEM images, the mean diameters of the obtained fcc- and hcp-RuIrPt NPs were 3.4 ± 0.4 nm and 3.2 ± 0.3 nm, respectively (Figure S24). For both types of alloy NPs, the metal compositions with the atomic ratio of Ru, Ir, and Pt were around 7:1.5:1.5 (Table S11).

The atomic resolution HAADF-STEM images and the relevant FFT patterns show the formation of an fcc structure of RuIrPt NPs including a typical fivefold-symmetry twinned structure (Figures 5a–c, and S25).[28] The observed lattice spacings were 2.22 Å, which is consistent with the results of Rietveld refinement (Figure 5c). The crystal structure of hcp-RuIrPt NPs was also confirmed by atomic resolution HAADF-STEM images and their FFT patterns (Figures 5d–f, and S26). Figure 5d shows the clear atomic arrangements with ABAB… stacking which is a typical hcp lattice viewed from the [010] direction. The (001) lattice spacing is 2.22 Å. These observed structures were also consistent with the ideal atomic arrangements constructed by the Rietveld refinement (Figure 5f). The solid-solution structures of fcc- and hcp-RuIrPt NPs were confirmed by EDX elemental maps and line scan analysis (Figures 5g–p, Figure S27). To the best of our knowledge, this is the first example of crystal structure control of multicomponent solid-solution alloy NPs. In addition, the XPS results suggested the electron transfer from Ru to Ir and Pt in both fcc and hcp alloys (Figure S28, Table S12). The compositions of RuIrPt NPs were also confirmed through the XPS peak area (Table S13). This example demonstrated that our crystal structure control strategy can be used in multicomponent alloy systems as well.

HER performance of the alloy catalysts. Platinum group metals are well-known effective electrocatalysts for HER, as well as the oxygen reduction and evolution reactions.[29–31] At present, although alkaline water electrolysis is an attractive method to produce clean hydrogen energy, the lower reaction rate of HER has hindered its application.[32,33] Ru based alloy nanomaterials are recently discovered as the promising catalysts for alkaline HER because of the suitable binding strength with hydrogen (~65 kcal mol^{-1}) and the lower water dissociation barrier of Ru.[34–36] Therefore, in this study, to investigate the effect of crystal structure on the catalytic performance of the solid-solution alloy NPs, the electrocatalytic HER in alkaline was investigated.

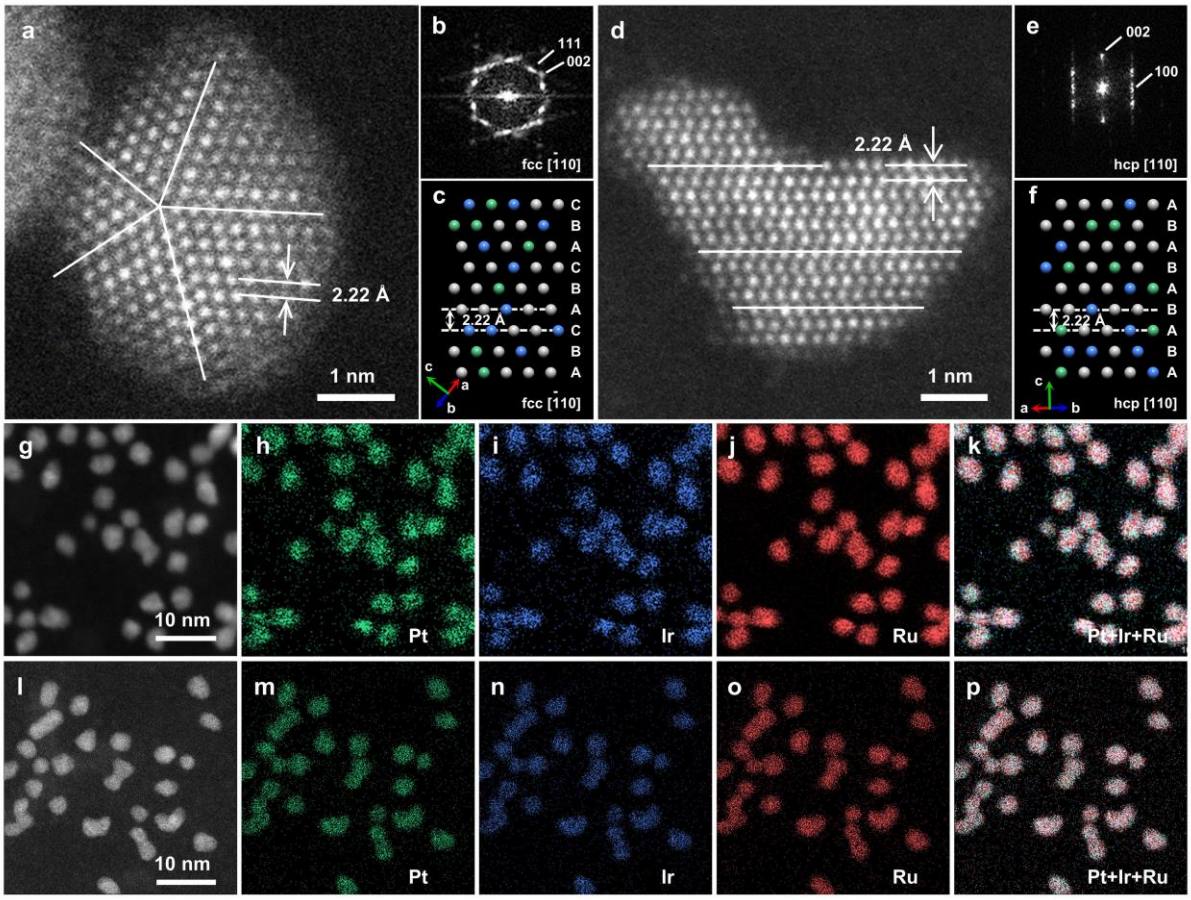

Figure 5. Structure characterization of fcc- and hcp-RuIrPt alloy NPs. **(a)** Atomic resolution HAADF-STEM image of an fcc-RuIrPt NP. The white lines in **(a)** show the twin boundaries. **(b)** The relevant fast Fourier transform (FFT) pattern of **(a)**. **(c)** Ideal fcc atomic arrangement constructed by the Rietveld refinement result. **(d)** Atomic resolution HAADF-STEM image of an hcp-RuIrPt NP. The white lines in **(d)** show the stacking faults. **(e)** The relevant FFT pattern of **(d)**. **(f)** Ideal hcp atomic arrangement constructed by the Rietveld refinement result. **(g)–(k), (l)–(p)** STEM-EDX maps of fcc- and hcp-RuIrPt alloy NPs.

We first prepared carbon-loaded alloy catalysts and estimated the electrochemically active surface area and active sites by the underpotential deposition of copper (Figures S29–S31, see the experimental details in Supporting Information). All the catalysts showed similar electrochemically active surface areas and active sites (Figures S32, S33). The HER performances of the catalysts were tested in a 1.0 M KOH solution. The linear sweep voltammetry (LSV) curves of the RuPt, RuIr and RuIrPt catalysts showed that the HER catalytic activities of all the alloys were higher compared with the monometallic catalysts (Figures 6a, d, g, and S34). Surprisingly, the hcp alloys showed a much better HER electrocatalytic activity than the fcc alloys. To achieve a current density of 10 mA cm^{-2}, the overpotentials for hcp- RuPt, RuIr, and RuIrPt were 12.9, 17.5, and 9.4 mV, respectively, much lower than those for fcc-RuPt (25.2 mV), RuIr (30.4 mV), and RuIrPt (23.3 mV), as well as commercial Pt/C (42.1 mV), Ir (87.9 mV), and Ru (48.1 mV) (Figure S35). Furthermore, the intrinsic activities of the catalysts were estimated from the TOF with the applied potentials. The hcp alloy catalysts also showed higher TOF values compared with the fcc alloy catalysts with the applied potentials (Figures 6b, e, h). The TOF values of hcp-RuPt, RuIr, and RuIrPt at 30 mV (2.35, 1.42, and 2.94 H_2 s^{-1}, respectively) were much larger than those of fcc-RuPt (0.92 H_2 s^{-1}), RuIr (0.62 H_2 s^{-1}), and RuIrPt (0.96 H_2 s^{-1}), commercial Pt/C (0.44 H_2 s^{-1}), Ir (0.18 H_2 s^{-1}), and Ru (0.35 H_2 s^{-1}) catalysts (Figures 6c, f, i, and S36). In particular, the TOF value of hcp-RuIrPt at an η of 30 mV was almost 3.1 and 6.7 times higher than those of the fcc-RuIrPt and commercial Pt/C, respectively. The HER mass catalytic activity of alloy NPs also confirmed that the hcp alloys showed much higher activity than the fcc alloys (Figure 6c, f, i, and S37). With an η of 30 mV, the current density of hcp-RuPt, RuIr, and RuIrPt (712.4, 433.2, and 877.5 A g^{-1}, respectively) were much higher than that of fcc-RuPt (263.2 A g^{-1}), RuIr (193.3 A g^{-1}), and RuIrPt (276.5 A g^{-1}), as well as the commercial Pt/C (127.8 A g^{-1}), Ir (54.8 A g^{-1}), and Ru (101.4 A g^{-1}) catalysts (Figures 6c, f, i, and S37). For hcp-RuIrPt, the mass activity at 30 mV was 3.2 and 6.9 times higher than that of fcc-RuIrPt and commercial Pt/C. The kinetic behavior of the electrocatalysts was evaluated by their Tafel slope (Figure S38). The lower Tafel slope values of the hcp alloys indicated that they had more favourable reaction kinetics during the HER process than the fcc alloys and monometallic catalysts. In addition, the LSV curves of the alloy catalysts after the durability test showed almost no or only a slight shift, indicating the excellent catalytic stability of the alloy catalysts (Figure S39).

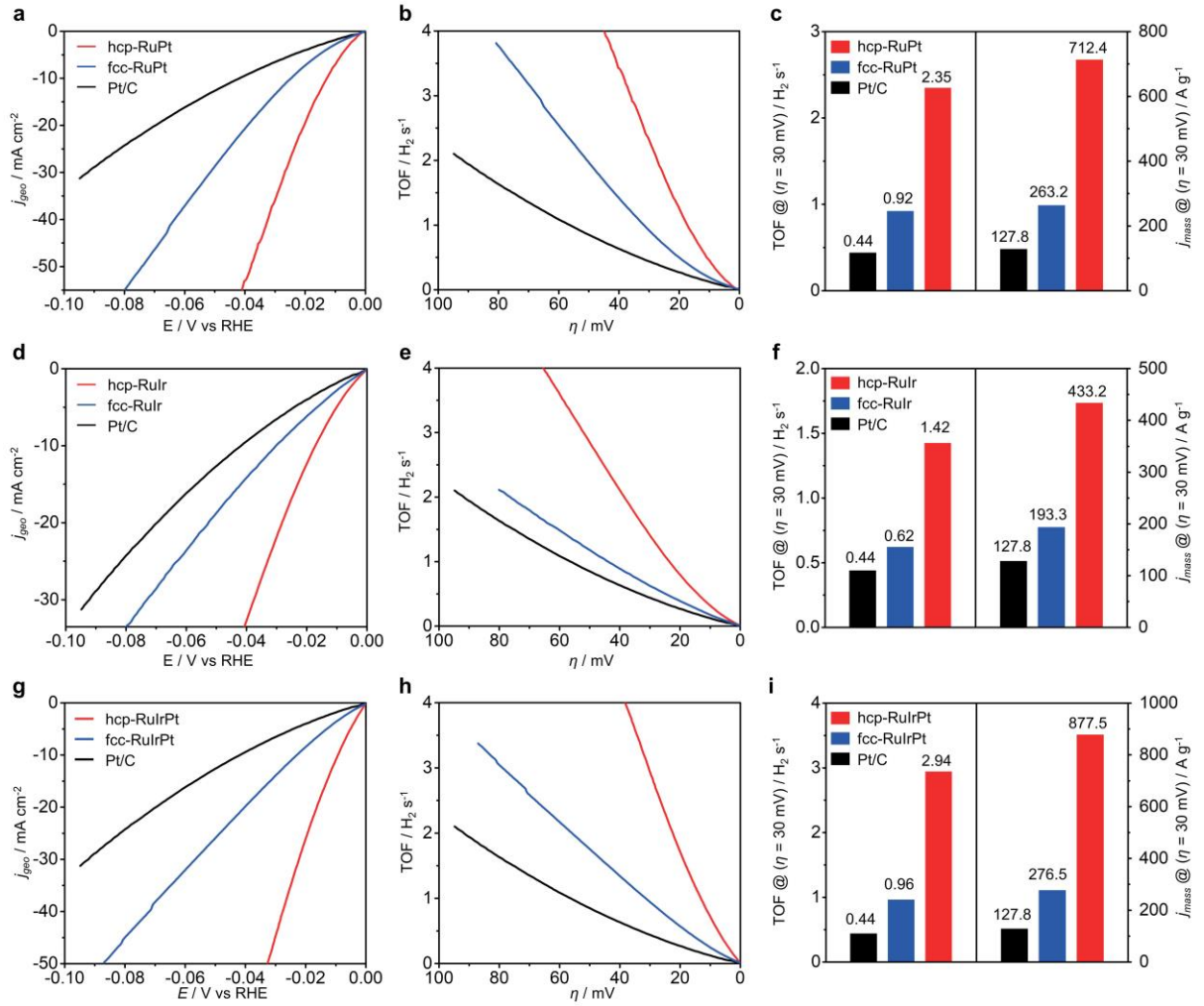

Figure 6. Crystal structure dependence of the HER catalytic performance in 1.0 M KOH. Polarization curves of fcc- and hcp-RuPt **(a)**, RuIr **(d)**, and RuIrPt **(g)**. TOF curves of fcc- and hcp-RuPt **(b)**, RuIr **(e)**, and RuIrPt **(h)**. TOF values (at an η of 30 mV) and mass activities (at an η of 30 mV) of fcc- and hcp-RuPt **(c)**, RuIr **(f)**, and RuIrPt **(i)**.

All these results demonstrated that the catalytic activity of the alloy catalysts strongly depended on their crystal structure. Regarding the HER in a 1.0 M KOH solution, the alloys with hcp structures showed a much higher activity than the alloys with fcc structures and were far superior to commercial Pt/C, Ir, and Ru. Remarkably, hcp-RuIrPt showed the best HER electrocatalytic activity, which is one of the best reported alloy catalysts for the alkaline HER (Figure S40, Table S14).

Considering the similar electrochemically active surface areas and active sites for alloy NPs with different crystal structures, the enhanced catalytic performance of alloy catalysts with the hcp structure is attributed to its intrinsic nature, which should be directly related to the crystal structure difference. The catalytic behavior is strongly related to the surface properties of a catalyst because the reactant and the intermediates are adsorbed on its surface.[37] Alloy NPs with different crystal structures definitely expose surfaces with different atomic arrangements and electronic structures.[38, 39] These geometric and electronic structure changes at the catalyst surface affect the adsorption behavior of reactants and intermediates, leading to different catalytic performance.[40] For HER in alkaline, the water dissociation, and OH and H adsorptions are the important factors that determine the overall activity.[41] The hcp alloys would show a better balance of the adsorption energies than the fcc alloys and finally induce enhanced HER catalytic performance.

CONCLUSION

In summary, by fine-tuning the reduction speed of metal precursors, we succeeded in selectively synthesizing fcc- and hcp- binary RuPt, RuIr and ternary RuIrPt solid-solution alloy NPs with the same compositions. All the alloy catalysts showed much improved catalytic performance toward HER in alkaline compared with monometallic catalysts. Hcp-RuIrPt recorded the best HER catalytic performances of alloy catalysts. Impressively, RuPt, RuIr, and RuIrPt with an hcp structure showed much higher electrocatalytic activities than these alloys with an fcc structure. This is the first systematic demonstration that the crystal structure significantly affected catalytic performance in solid-solution alloy NPs. Given the broad scope of applications for alloy NPs, it is considered that the crystal structure control strategy can be applied not only for alloy catalysts but also for other alloy nanomaterials

such as nanomagnets. The present work will inspire the exploration of new inorganic materials with interesting properties through crystal structure control.

ASSOCIATED CONTENT

Supporting Information.
The Supporting Information is available free of charge at http://pubs.acs.org.
Experimental details, TEM images, Rietveld refinement analysis of the powder XRD patterns, in-situ XRD results, EDX line scan profiles, STEM images, XPS spectra, UV−vis spectra, and results of electrochemical measurements (Figures S1−S40 and Tables S1−S14) (PDF)

AUTHOR INFORMATION

Corresponding Authors

Quan Zhang -- Division of Chemistry, Graduate School of Science, Kyoto University, Kitashirakawa-Oiwakecho, Sakyo-ku, Kyoto 606-8502, Japan; Email: zhangquan2014@kuchem.kyoto-u.ac.jp

Kohei Kusada -- Division of Chemistry, Graduate School of Science, Kyoto University, Kitashirakawa-Oiwakecho, Sakyo-ku, Kyoto 606-8502, Japan; Present Address: The Hakubi Center for Advanced Research, Kyoto University, Kitashirakawa-Oiwakecho, Sakyo-ku, Kyoto 606−8502, Japan; Email: kusada@kuchem.kyoto-u.ac.jp

Hiroshi Kitagawa -- Division of Chemistry, Graduate School of Science, Kyoto University, Kitashirakawa-Oiwakecho, Sakyo-ku, Kyoto 606-8502, Japan; Email: kitagawa@kuchem.kyoto-u.ac.jp

Authors

Dongshuang Wu -- Division of Chemistry, Graduate School of Science, Kyoto University, Kitashirakawa-Oiwakecho, Sakyo-ku, Kyoto 606-8502, Japan;

Tomokazu Yamamoto -- The Ultramicroscopy Research Centre, Kyushu University, Motooka 744, Nishi-ku, Fukuoka 819-0395, Japan;

Takaaki Toriyama -- The Ultramicroscopy Research Centre, Kyushu University, Motooka 744, Nishi-ku, Fukuoka 819-0395, Japan;

Syo Matsumura -- The Ultramicroscopy Research Centre, Kyushu University, Motooka 744, Nishi-ku, Fukuoka 819-0395, Japan; Department of Applied Quantum Physics and Nuclear Engineering, Kyushu University, 744 Motooka, Nishi-ku, Fukuoka 819-0395, Japan;

Shogo Kawaguchi -- Japan Synchrotron Radiation Research Insitute (JASRI), SPring-8, 1-1-1 Kouto, Sayo-cho, Sayo-gun, Hyogo 679-5198, Japan;

Yoshiki Kubota -- Department of Physical Science, Graduate School of Science, Osaka Prefecture University, Sakai, Osaka 599-8531, Japan;

Notes

The authors declare no competing interest.

ACKNOWLEDGMENTS

The authors acknowledge the support from the JST ACCEL program grant No. JPMJAC1501 and the MEXT KAKENHI Grant-in-Aid for Specially Promoted Research 20H05623. STEM observations were performed as part of a program conducted by the Advanced Characterization Nanotechnology Platform sponsored by the Ministry of Education, Culture, Sports, Science and Technology (MEXT) of the Japanese government. Synchrotron XRD measurements were performed at SPring-8 under proposals No. 2021A1204 and No. 2020A1162.

REFERENCES

(1) COX, P. A. *The Electronic Structure and Chemistry of Solids*; Oxford University Press, 1987; pp 45−129.

(2) Novoselov, K. S.; Geim, A. K.; Morozov, S. V.; Jiang, D.; Zhang, Y.; Dubonos, S. V.; Grigorieva, I. V.; Firsov, A. A. Electric Field Effect in Atomically Thin Carbon Films. *Science* **2004**, *306* (5696), 666–669.

(3) Kakehashi, Y.; Jepsen, O.; Kimura, N. Ground-State Electronic Structure Calculations of the Multiple Spin-Density-Wave State in γ-Fe. *Phys. Rev. B.* **2002**, *65* (13), 134418.

(4) Sun S.; Murray, C. B.; Weller, D.; Folks, L.; Moser. A. Monodisperse FePt Nanoparticles and Ferromagnetic FePt Nanocrystal Superlattices. *Science* **2000**, *287* (5460), 1989–1992.

(5) Kim, D.; Xie, C.; Becknell, N.; Yu, Y.; Karamad, M.; Chan, K.; Crumlin, E. J.; Nørskov, J. K.; Yang, P. Electrochemical Activation of CO_2 through Atomic Ordering Transformations of AuCu Nanoparticles. *J. Am. Chem. Soc.* **2017**, *139* (24), 8329–8336.

(6) Yun, Q.; Lu, Q.; Li, C.; Chen, B.; Zhang, Q.; He, Q.; Hu, Z.; Zhang, Z.; Ge, Y.; Yang, N.; Ge, J.; He, Y.; Gu, L.; Zhang, H. Synthesis of PdM (M = Zn, Cd, ZnCd) Nanosheets with an Unconventional Face-Centered Tetragonal Phase as Highly Efficient Electrocatalysts for Ethanol Oxidation. *ACS Nano* **2019**, *13* (12), 14329–14336.

(7) Li, Z.; Saruyama, M.; Asaka, T.; Tatetsu, Y.; Teranishi, T. Determinants of Crystal Structure Transformation of Ionic Nanocrystals in Cation Exchange Reactions. *Science* **2021**, *373* (6552), 332–337.

(8) Zhou, M.; Liu, J.; Ling, C.; Ge, Y.; Chen, B.; Tan, C.; Fan, Z.; Huang, J.; Chen, J.; Liu, Z.; Huang, Z.; Ge, J.; Cheng, H.; Chen, Y.; Dai, L.; Yin, P.; Zhang, X.; Yun, Q.; Wang, J.; Zhang, H. Synthesis of Pd_3Sn and PdCuSn Nanorods with $L1_2$ Phase for Highly Efficient Electrocatalytic Ethanol Oxidation. *Adv. Mater.* **2022**, *34* (1), 2106115.

(9) Kobayashi, H.; Kusada, K.; Kitagawa, H. Creation of Novel Solid-Solution Alloy Nanoparticles on the Basis of Density-of-States Engineering by Interelement Fusion. *Acc. Chem. Res.* **2015**, *48* (6), 1551–1559.

(10) Gilroy, K. D.; Ruditskiy, A.; Peng, H.; Qin, D.; Xia, Y. Bimetallic Nanocrystals: Syntheses, Properties, and Applications. *Chem. Rev.* **2016**, *116* (18), 10414–10472.

(11) Kim, D.; Resasco, J.; Yu, Y.; Asiri, A. M.; Yang, P. Synergistic Geometric and Electronic Effects for Electrochemical Reduction of Carbon Dioxide Using Gold–Copper Bimetallic nanoparticles. *Nat. Commun.* **2014**, *5*, 4948.

(12) Yao, Y.; Huang, Z.; Xie, P.; Lacey, S. D.; Jacob, R. J.; Xie, H.; Chen, F.; Nie, A.; Pu, T.; Regwoldt, M.; Yu, D.; Zachariah, M. R.; Wang, C.; Shahbazian-Yassar, R.; Li, J.; Hu, L. Carbothermal Shock Synthesis of High-Entropy-Alloy Nanoparticles. *Science* **2018**, *359* (6383), 1489–1494.

(13) Luo, M.; Zhao, Z.; Zhang, Y.; Sun, Y.; Xing, Y.; Lv, F.; Yang, Y.; Zhang, X.; Hwang, S.; Qin, Y.; Ma, J.; Lin, F.; Su, D.; Lu, G.; Guo, S. PdMo Bimetallene for Oxygen Reduction Catalysis. *Nature* **2019**, *574*, 81–85.

(14) Massalski, T. B.; Okamoto, H.; Subramanian, P. R.; Kacprzak, L. *Binary Alloy Phase Diagrams,* 2nd Ed.; ASM International, 1990; pp 410−2345.

(15) Ge, Y.; Wang, X.; Huang, B.; Huang, Z.; Chen, B.; Ling, C.; Liu, J.; Liu, G.; Zhang, J.; Wang, G.; Chen, Y.; Li, L.; Liao, L.; Wang, L.; Yun, Q.; Lai, Z.; Lu, S.; Luo, Q.; Wang, J.; Zheng, Z.; Zhang, H. Seeded Syn-

thesis of Unconventional 2H-Phase Pd Alloy Nanomaterials for Highly Efficient Oxygen Reduction. *J. Am. Chem. Soc.* **2021**, *143* (41), 17292–17299.

(16) Liu, J.; Huang, J.; Niu, W.; Tan, C.; Zhang, H. Unconventional-Phase Crystalline Materials Constructed from Multiscale Building Blocks. *Chem. Rev.* **2021**, *121* (10), 5830–5888.

(17) Zhang, Q.; Kusada, K.; Kitagawa, H. Phase Control of Noble Monometallic and Alloy Nanomaterials by Chemical Reduction Methods. *ChemPlusChem* **2021**, *86* (3), 504–519.

(18) Kawaguchi, S.; Takemoto, M.; Osaka, K.; Nishibori, E.; C. Moriyoshi, C.; Kubota, Y.; Kuroiwa, Y.; Sugimoto, K. High-Throughput Powder Diffraction Measurement System Consisting of Multiple MYTHEN Detectors at Beamline BL02B2 of SPring-8. *Rev. Sci. Instrum.* **2017**, *88* (8), 085111.

(19) Denton, A. R.; Ashcroft, N. W. Vegard's Law. *Phy. Rev. A* **1991**, *43* (6), 3161–3164.

(20) Kusada, K.; Kobayashi, H.; Ikeda, R.; Kubota, Y.; Takata, M.; Toh, S.; Yamamoto, T.; Matsumura, S.; Sumi, N.; Sato, K.; Nagaoka, K.; Kitagawa, H. Solid Solution Alloy Nanoparticles of Immiscible Pd and Ru Elements Neighboring on Rh: Changeover of the Thermodynamic Behavior for Hydrogen Storage and Enhanced CO-Oxidizing Ability. *J. Am. Chem. Soc.* **2014**, *136* (5), 1864–1871.

(21) Wu, D.; Cao, M.; Shen, M.; Cao, R. Sub-5 nm Pd-Ru Nanoparticle Alloys as Efficient Catalysts for Formic Acid Electrooxidation. *ChemCatChem* **2014**, *6* (6), 1731–1736.

(22) Zhang, Q.; Kusada, K.; Wu, D.; Ogiwara, N.; Yamamoto, T.; Toriyama, T.; Matsumura, S.; Kawaguchi, S.; Kubota, Y.; Honma, T.; Kitagawa, H. Solid-Solution Alloy Nanoparticles of a Combination of Immiscible Au and Ru with a Large Gap of Reduction Potential and their Enhanced Oxygen Evolution Reaction Performance, *Chem. Sci.*, **2019**, *13* (10), 5133–5137.

(23) Zhang, Q.; Kusada, K.; Wu, D.; Yamamoto, T.; Toriyama, T.; Matsumura, S.; Kawaguchi, S.; Kubota, Y.; Kitagawa, H. Selective Control of Fcc and Hcp Crystal Structures in Au–Ru Solid-Solution Alloy Nanoparticles. *Nat. Commun.* **2018**, *9*, 510.

(24) Zhou, M.; Wang, H.; Vara, M.; Hood, Z. D.; Luo, M.; Yang, T.; Bao, S.; Chi, M.; Xiao, P.; Zhang, Y.; Xia, Y. Quantitative Analysis of the Reduction Kinetics Responsible for the One-Pot Synthesis of Pd–Pt Bimetallic Nanocrystals with Different Structures. *J. Am. Chem. Soc.* **2016**, *138* (37), 12263–12270.

(25) Wu, D.; Zheng, Z.; Gao, S.; Cao, M.; Cao, R. Mixed-Phase PdRu Bimetallic Structures with High Activity and Stability for Formic Acid Electrooxidation. *Phys. Chem. Chem. Phys.* **2012**, *14* (22), 8051–8057.

(26) Wang, H.; Chen, Z.; Wu, D.; Cao, M.; Sun, F.; Zhang, H.; You, H.; Zhuang, W.; Cao, R. Significantly Enhanced Overall Water Splitting Performance by Partial Oxidation of Ir through Au Modification in Core–Shell Alloy Structure. *J. Am. Chem. Soc.* **2021**, *143* (12), 4639–4645.

(27) LaMer, V. K.; Dinegar, R. H. Theory, Production and Mechanism of Formation of Monodispersed Hydrosols. *J. Am. Chem. Soc.* **1950**, *72* (11), 4847-4854.

(28) Chen, C.; Zhu, C.; White, E. R.; Chiu, C.; Scott, M. C.; Regan, B. C.; Marks, L. D.; Huang, Y.; Miao, J. Three-Dimensional Imaging of Dislocations in a Nanoparticle at Atomic Resolution. *Nature* **2013**, 496, 74–77.

(29) Mahmood, J.; Li, F.; Jung, S.; Okyay, M. S.; Ahmad, I.; Kim, S.; Park, N.; Jeong, H. Y.; Baek, J. An Efficient and PH-Universal Ruthenium-Based Catalyst for the Hydrogen Evolution Reaction. *Nat. Nanotechnol.* **2017**, *12*, 441–446.

(30) Garlyyev, B.; Kratzl, K.; Rück, M.; Michalička, J.; Fichtner, J.; Macak, J. M.; Kratky, T.; Ggnther, S.; Cokoja, M.; Bandarenka, A. S.; Gagliardi, A.; Fischer, R. A. Optimizing the Size of Platinum Nanoparticles for Enhanced Mass Activity in the Electrochemical Oxygen Reduction Reaction. *Angew. Chem. Int. Ed.* **2019**, *58* (28), 9596 –9600.

(31) Wang, J.; Han, L.; Huang, B.; Shao, Q.; Xin, H. L.; Huang, X. Amorphization Activated Ruthenium-Tellurium Nanorods for Efficient Water Splitting. *Nature Commun.* **2019**, 10, 5692.

(32) Sheng, W.; Gasteiger, H. A.; Shao-Horn, Y. Hydrogen Oxidation and Evolution Reaction Kinetics on Platinum: Acid vs Alkaline Electrolytes. *J. Electrochem. Soc.* **2010**, *157* (11), B1529–B1536.

(33) Rheinländer, P. J.; Herranz, J.; Durst, J.; Gasteiger, H. A. Kinetics of the Hydrogen Oxidation/Evolution Reaction on Polycrystalline Platinum in Alkaline Electrolyte Reaction Order with Respect to Hydrogen Pressure. *J. Electrochem. Soc.* **2014**, *161* (14), F1448–F1457.

(34) Zhang, S.; Li, J.; Wang, E. Recent Progress of Ruthenium-based Nanomaterials for Electrochemical Hydrogen Evolution. *ChemElectroChem* **2020**, *7* (22), 4526–4534.

(35) Mitchell, W. J.; Xie, J.; Jachimowski, T. A.; Weinberg, W. H. Carbon Monoxide Hydrogenation on the Ru(001) Surface at Low Temperature Using Gas-Phase Atomic Hydrogen: Spectroscopic Evidence for the Carbonyl Insertion Mechanism on a Transition Metal Surface. *J. Am. Chem. Soc.* **1995**, *117* (9), 2606–2617.

(36) Feibelman, P. J. Partial Dissociation of Water on Ru(0001). *Science* **2002**, *295* (5552), 99–102.

(37) Zheng, Y.; Jiao, Y.; Jaroniec, M.; Qiao, S. Advancing the Electrochemistry of the Hydrogen-Evolution Reaction through Combining Experiment and Theory. *Angew. Chem. Int. Ed.* **2015**, *54* (1), 52–65.

(38) Zhao P.; Cao, Z.; Liu, X.; Ren, P.; Cao, D.; Xiang, H.; Jiao, H.; Yang, Y.; Li, Y.; Wen, X. Morphology and Reactivity Evolution of HCP and FCC Ru Nanoparticles under CO Atmosphere. *ACS Catal.* **2019**, *9* (4), 2768–2776.

(39) Liu J.; Su, H.; Sun, D.; Zhang, B.; Li, W. Crystallographic Dependence of CO Activation on Cobalt Catalysts: HCP versus FCC. *J. Am. Chem. Soc.* **2013**, *135* (44), 16284–16287.

(40) Zheng, Y.; Jiao, Y.; Zhu, Y.; Li, L. H.; Han, Y.; Chen, Y.; Jaroniec, M.; Qiao, S. High Electrocatalytic Hydrogen Evolution Activity of an Anomalous Ruthenium Catalyst. *J. Am. Chem. Soc.* **2016**, *138* (49), 16174–16181.

(41) Subbaraman, R.; Tripkovic, D.; Strmcnik, D.; Chang, K.; Uchimura, M.; Paulikas, A. P.; Stamenkovic, V.; Markovic, N. M. Enhancing Hydrogen Evolution Activity in Water Splitting by Tailoring Li^+–$Ni(OH)_2$–Pt Interfaces. *Science* **2011**, *334* (6060), 1256–1260.

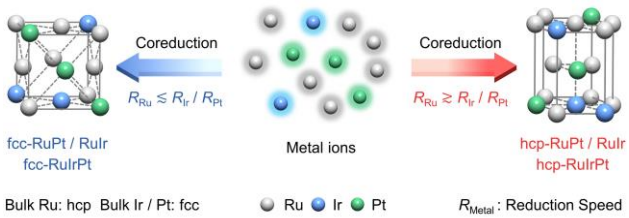
Coreduction
$R_{Ru} \lesssim R_{Ir} / R_{Pt}$
fcc-RuPt / RuIr
fcc-RuIrPt
Metal ions
Coreduction
$R_{Ru} \gtrsim R_{Ir} / R_{Pt}$
hcp-RuPt / RuIr
hcp-RuIrPt
Bulk Ru: hcp Bulk Ir / Pt: fcc
Ru Ir Pt
R_{Metal} : Reduction Speed